Multi-Yield Surface Modeling of Viscoplastic Materials

Hao Yan and Caglar Oskay*

Department of Civil and Environmental Engineering
Vanderbilt University
Nashville, TN 37235

Abstract

This manuscript presents a multi-yield surface model to idealize the mechanical behavior of viscoplastic solids subjected to cyclic loading. The multi-yield surface model incorporates the evolution of nonlinear viscoplastic flow through a piece-wise linear hardening approximation. A kinematic hardening law is employed to account for the evolution of backstress with respect to the viscoplastic strain rate. The new backstress evolution strategy is proposed to ensure that all yield surfaces remain consistent (i.e., satisfying collinearity) throughout the viscoplastic process. The multi-yield surface model is coupled with viscoelasticity to approximate the relaxation behavior of high temperature metal alloys. The model is implemented using a mixed finite element approach. The capabilities of the proposed approach are demonstrated using experiments conducted on a high temperature titanium alloy (Ti-6242S) subjected to static, cyclic and relaxation conditions.

Keywords: Multi-yield surface plasticity; Viscoelastic-viscoplastic behavior; Cyclic loading.

1 Introduction

Modeling the cyclic response of materials in the presence of material nonlinearity is critical for many engineering applications, ranging from soils and soil-structure systems under

*Corresponding author address: VU Station B#351831, 2301 Vanderbilt Place, Nashville, TN 37235. Email: caglar.oskay@vanderbilt.edu

earthquake excitations to metals subjected to low cycle fatigue. In this manuscript, we are particularly concerned with modeling the cyclic response in the presence of viscous effects for analysis of structures subjected to mechanical loading at elevated temperatures. The proposed cyclic modeling approach contributes to multiscale modeling in two ways: (a) In the context of multiple time scale homogenization schemes to characterize the long term degradation of structural components; and (b) in providing a flexible constitutive framework for sequential multiscale modeling.

In order to address the presence of multiple time scales, the long term performance of structures subjected to cyclic loading are traditionally modeled using cycle-jump approaches (see e.g., [11]). More recently, an alternative methodology based on the multiple time scale computational homogenization has been developed by Oskay and Fish [29, 30] to investigate the failure behavior of a range of materials from metals [30, 16] to composites [13, 14, 3]. The multiple time scale methodology, as well as the cycle-jump approaches rely on accurate evaluation of a select fully-discretized load cycles throughout the life of a structure or a component. In addressing the presence of multiple length scales, sequential multiscale modeling is a promising approach to evaluate the thermo-mechanical behavior of such complex materials in a computationally efficient manner. In sequential multiscale modeling, the premise is to calibrate a macroscale constitutive form based on a large suite of detailed fine scale simulations that accurately describe the nonlinear behavior of the material within a range of load conditions. This approach clearly rely on the availability of flexible constitutive forms that can conform to data resulting from the fine scale calculations. The present effort is to devise such a constitutive form for viscoplastic cyclic thermo-mechanical behavior.

Modeling of the cyclic response of metals at high temperature has seen significant advances in the past few decades, which have been summarized in thorough literature surveys such as by McDowell [26] and Chaboche [7]. Beyond the crystal plasticity based cyclic deformation models (e.g., [5, 21, 25]), the majority of phenomenological plasticity models rely on the concept of a yield surface, typically defined in the stress space, as well as evolution laws for internal state variables (ISVs) consistently derived from thermodynamics principles. Those deformation mechanisms pertinent to the high temperature environments are incorporated using complex functional relationships into the evolution laws of the ISVs. Starting

from the foundational models of Prager [32] and Ziegler [39], comprehensive ISV formulations for cyclic plasticity, incorporating time- and rate-dependent effects have been developed, including the models of Chaboche [6] and Frederick and Armstrong [17], application of the viscoplasticity theory based on overstress [22], ratcheting models [28, 2, 19], among many others.

An alternative approach, named multi-yield surface plasticity (MYSP), was originally proposed by Mroz *et al.* [27] and further developed for soil plasticity by Prevost and coworkers (e.g., [33, 34, 35]), as well as metal plasticity [12]. In multi-yield surface plasticity, multiple, non-intersecting yield surfaces are employed to define the evolution of the plastic flow. In this approach, the behavior is approximated as linearly hardening between two neighboring yield surfaces, leading to a piecewise linear approximation of the plastic flow. The evolution equations are therefore very simple and the accuracy is controlled by the number of yield surfaces used. Elgamal *et al.* [15, 18] proposed a modification to Mroz's multi-yield surface model, in order to reduce the computational cost by redefining the backstress translation direction. Chiang [9] proposed a new description of the unloading and reloading processes in MYSP by applying a transformation to the stress state. A new hardening rule, based on the superposition of Mroz's and Ziegler's rule in the context of a two-surface model, was presented by Chen [8]. Choi and Pan [10] derived a generalized anisotropic hardening rule based on MYSP for pressure insensitive and sensitive materials. The available literature in multi-yield surface plasticity primarily focuses on the rate independent behavior, where dissipation is often introduced as structural damping. To the best of the authors' knowledge, no attempt has been made so far to introduce rate effects at the material level.

In this manuscript, a multi-yield surface model is proposed to idealize the mechanical behavior of viscoplastic solids subjected to cyclic loading. The proposed approach builds on the classical MYSP model [27] by extending it to account for the viscoplastic behavior, which is critical for the response characterization of metals and alloys at high temperatures. The effect of rate dependent behavior on the evolution of the backstress is induced without violating the collinearity rule. The model is implemented using a mixed finite element approach, in which the displacement and pressure are evaluated as independent unknowns [36, 37]. The capabilities of the model are assessed by simulating the experimentally observed behavior

of the high temperature titanium alloy, Ti-6242S subjected to static, cyclic and relaxation conditions. The main contribution of this manuscript is the extension of the multi-yield surface plasticity approach to the viscoplastic regime. The flexibility of the present approach in capturing the cyclic behavior makes it attractive for sequential multiscale modeling of plastic deformation, where MYSP serves as the macroscale material model calibrated using lower scale (e.g., polycrystal plasticity) simulations.

The remainder of this manuscript is organized as follows: Section 2 introduces the background and the basic theory of the multi-yield surface plasticity. The proposed multi-yield surface viscoplasticity model is explained in Section 3. Section 4 presents the combined viscoelastic-viscoplastic constitutive model used to describe high temperature behavior of some metal alloys. Section 5 presents the mixed finite element implementation. Section 6 details a numerical investigation of the cyclic behavior of Ti-6242S at elevated temperatures. The conclusion and future research directions are provided in Section 7.

2 Overview of multi-yield surface plasticity

In this section, Mroz's multi-yield surface plasticity model [27], which is the starting point of the proposed model, is summarized. In Mroz's formulation, a series of yield surfaces are defined, each of which is associated with a unique plastic moduli, a yield stress and a backstress to describe the piecewise linear, elasto-plastic, rate independent constitutive behavior.

Consider M yield surfaces to approximate the elastoplastic behavior as illustrated in Fig. 1, where S_1, S_2, S_3 are deviatoric stresses invariants and S_I, S_{II}, S_{III} are principal deviatoric stresses. The yield surfaces are taken to be initially concentric, indicating the assumed initial isotropy of yielding. The yield surfaces are ordered according to their sizes in the π-plane as shown in Fig. 1a. For simplicity, each yield surface is modeled using the Von-Mises yield function (Fig. 1b). The extension to more complex yield shapes, as well as pressure-dependent yielding has been previously proposed [20]. An arbitrary yield function is expressed as:

$$f^m\left(\boldsymbol{\sigma}, \boldsymbol{\alpha}^m; \sigma_Y^m\right) := \sqrt{3}\bar{s}^m\left(\boldsymbol{\sigma}, \boldsymbol{\alpha}^m\right) - \sigma_Y^m \leqslant 0; \quad m = 1, 2, ..., M \tag{1}$$

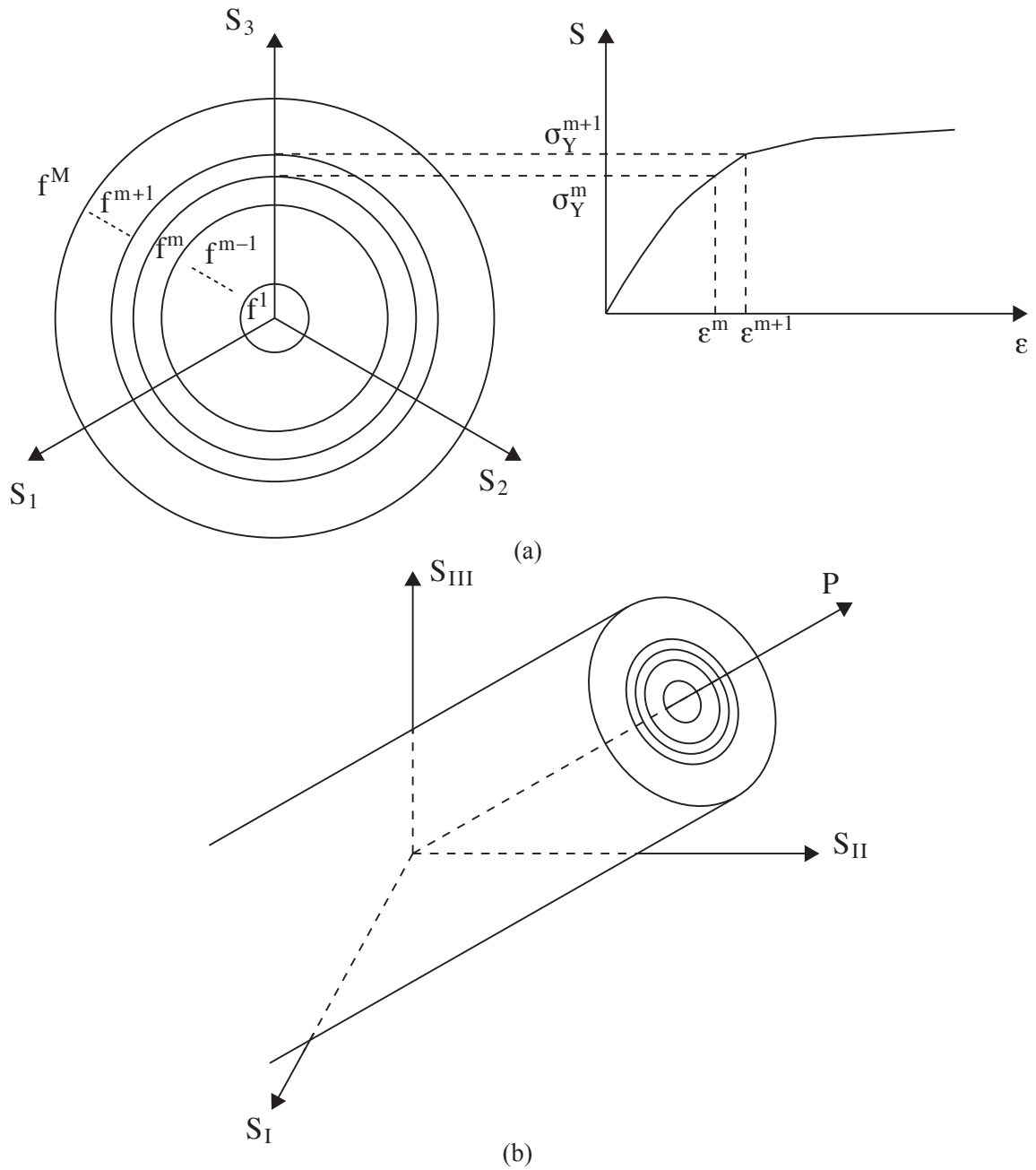

Figure 1: Yield surfaces of multi yield surface J2 plasticity model in (a) the deviatoric stress space; and (b) the principal stress space.

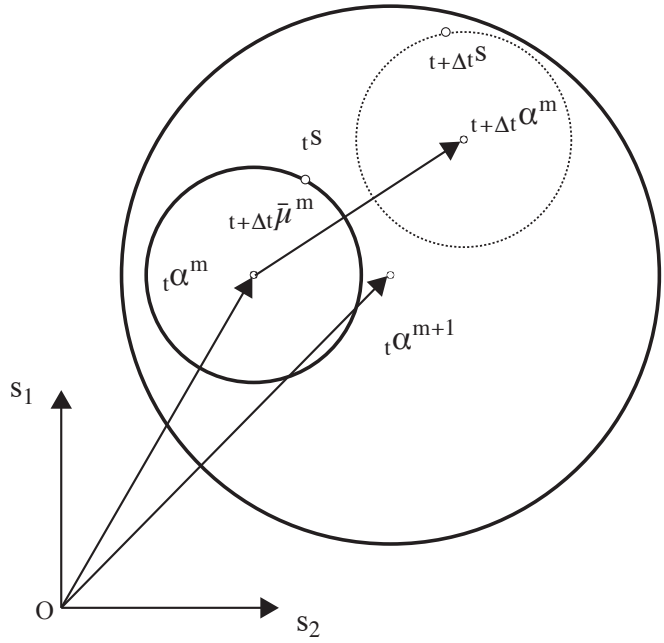

Figure 2: Mroz's deviatoric hardening evolution.

where, σ_Y^m is the flow stress of the mth yield surface; f^m the mth yield function. Symbols with bold fonts indicate tensor notation. $\bar{s}^m$ is the second invariant of the difference between the deviatoric stress, $\mathbf{s} = \boldsymbol{\sigma} - tr\left(\boldsymbol{\sigma}\right)/3$, ($tr(.)$ denotes the trace of a tensor) and the backstress $\boldsymbol{\alpha}^m$ of the mth yield surface:

$$\bar{s}^m = \sqrt{\frac{1}{2}\left(s_{ij} - \alpha_{ij}^m\right)\left(s_{ij} - \alpha_{ij}^m\right)} \tag{2}$$

In what follows, the index notation is adopted in the formulation of the model unless otherwise indicated, $i = 1, ..., n_{\text{sd}}$, where n_{sd} is the number of spatial dimensions. Repeated indices of the spatial dimensions indicate summation unless otherwise stated. A subscript followed by a comma indicates partial derivative (i.e., $f_{,i} = \partial f/\partial x_i$) and the dummy index m is reserved for variables associated with the mth yield surface.

In multi-yield surface plasticity, a pure kinematic hardening rule is typically employed. As illustrated in Fig. 2, each yield surface undergoes rigid body translation in the stress space towed by the deviatoric stress tensor. The magnitude and orientation of each yield surface remain unaltered for constant temperature. The shifting of the yield surfaces are performed such that none of the yield surfaces intersect another (i.e., collinearity condition [27]). Let $\hat{m}$

denote the *current* active yield surface at an arbitrary equilibrium state, defined as follows:

$$f^m = 0 \ \forall \ m = 1, 2, ..., \hat{m}; \ \text{ and } \ f^{\hat{m}+1} < 0 \tag{3}$$

The associative flow rule is used to define the evolution of the plastic strain, which follows the direction of the outward normal to the current active yield surface at the stress point [18, 35]:

$$Q_{ij}^{\hat{m}} = \frac{1}{Q^{\hat{m}}} \frac{\partial f^{\hat{m}}}{\partial s_{ij}} \tag{4}$$

where:

$$Q^{\hat{m}} = \sqrt{\frac{\partial f^{\hat{m}}}{\partial s_{ij}} \frac{\partial f^{\hat{m}}}{\partial s_{ij}}} \tag{5}$$

Employing the standard complementary and consistency conditions defined on the current active yield surface, the magnitude of the slip rate is computed as:

$$L^{\hat{m}} = \frac{1}{H^{\hat{m}}} Q_{ij}^{\hat{m}} \dot{s}_{ij} \tag{6}$$

where $H^{\hat{m}}$ is the plastic modulus associated with the current active yield surface. Then the evolution of the plastic strain, $\dot{\boldsymbol{\varepsilon}}^p$ is defined as:

$$\dot{\varepsilon}_{ij}^p = \left\langle L^{\hat{m}} \right\rangle Q_{ij}^{\hat{m}} \tag{7}$$

in which, $\langle \cdot \rangle$ denotes the Macaulay brackets (i.e., $\langle \cdot \rangle = ((\cdot) + | \cdot |)/2$).

We consider a pure deviatoric kinematic hardening rule:

$$\dot{\boldsymbol{\alpha}}^{\hat{m}} = \| \dot{\boldsymbol{\alpha}}^{\hat{m}} \| \boldsymbol{\mu}^{\hat{m}} \tag{8}$$

where the magnitude of the translation $\| \dot{\boldsymbol{\alpha}}^{\hat{m}} \|$ of the current active yield surface satisfies the consistency condition and the normalized translation direction $\mu_{ij}^{\hat{m}}$ as proposed by Mroz [27]) for elasto-plastic materials. As shown in Fig. 2, the translation tensor $\bar{\mu}_{ij}^{\hat{m}}$ for current

active yield surface $\hat{m}$ is defined as:

$$\bar{\boldsymbol{\mu}}^{\hat{m}} = \frac{\sigma_Y^{\hat{m}+1}}{\sigma_Y^{\hat{m}}} \left(\boldsymbol{s} - \boldsymbol{\alpha}^{\hat{m}}\right) - \left(\boldsymbol{s} - \boldsymbol{\alpha}^{\hat{m}+1}\right) \tag{9}$$

and the normalized direction is:

$$\boldsymbol{\mu}^{\hat{m}} = \frac{\bar{\boldsymbol{\mu}}^{\hat{m}}}{\|\bar{\boldsymbol{\mu}}^{\hat{m}}\|} \tag{10}$$

The translation direction in Eq. 9 ensures that the yield surfaces $\hat{m}$ and $\hat{m}+1$ do not overlap. All *inner* yield surfaces are translated in the same fashion and are tangent to the current active yield surface at the current stress point.

3 Multi-yield surface viscoplasticity

In this manuscript, we propose a new formulation that extends Mroz's rate-independent plasticity model into the rate-dependent regime. The relationship between the evolution of backstress and viscoplastic strain is replaced by a general form that guarantees the collinearity condition [24].

We posit the existence of a viscoplastic potential defined as a function of all yield surfaces, i.e., $\Omega\left(f^1, f^2, ..., f^M\right)$. The evolution of viscoplastic strain is expressed as [7]:

$$\dot{\varepsilon}_{ij}^{vp} = \sum_{m=1}^{M} \frac{\partial \Omega}{\partial f^m} \frac{\partial f^m}{\partial \sigma_{ij}} \tag{11}$$

It is convenient to consider a generalization of the Perzyna law in order to specify the viscoplastic potential. Let the viscoplastic potential consist of the additive sum of the contributions from the viscoplastic potential associated with each yield surface:

$$\Omega\left(f^1, f^2, ..., f^M\right) = \sum_{m=1}^{M} \Omega^m\left(f^m\right) \tag{12}$$

in which:

$$\Omega^m = \frac{\gamma \sigma_Y^m}{q+1} \left\langle \frac{f^m}{\sigma_{Y^m}} \right\rangle^{q+1} \tag{13}$$

where, γ and q denote the fluidity and viscoplastic hardening parameters, respectively. The

resulting flow rule becomes:

$$\dot{\varepsilon}_{ij}^{vp} = \sum_{m=1}^{M} \gamma \left\langle \frac{f^m}{\sigma_{Y^m}} \right\rangle^q \frac{\partial f^m}{\partial \sigma_{ij}} \tag{14}$$

Substituting Eq. 1 into Eq. 14:

$$\frac{\partial f^m}{\partial \sigma_{ij}} = \frac{\sqrt{3}}{2\bar{s}^m} \left(s_{ij} - \alpha_{ij}^m \right) \tag{15}$$

The formulation of the hardening evolution equations for each yield surface requires special attention since it differs significantly from rate-independent multi-yield surface plasticity. We adopt a simple pure kinematic piecewise linear hardening law, following Prager's model. In the context of single yield surface plasticity, the evolution of the backstress is expressed as:

$$\dot{\alpha}_{ij} = C\dot{\varepsilon}_{ij}^{vp} \tag{16}$$

where C is the plastic modulus. The direction of translation of a yield surface is shown in Eq. 10.

It is important to note that in contrast to rate independent plasticity the stress state does not have to lie within or on the current active yield surface, $\hat{m}$, when the rate effect is included. For instance, in case of a creep test where the stress state remains unaltered, all yield surfaces within the active yield surface (i.e., $1 < m \leqslant \hat{m}$) continue to translate with respect to each other until eventually reaching a steady state (i.e., image stress) at t=∞. At the asymptote, all yield surfaces become tangent to each other.

We adopt a form similar to the Prager's rule to describe hardening evolution for the current active yield surface, $\hat{m}$:

$$\dot{\alpha}_{ij}^{\hat{m}} = \hat{C}^{\hat{m}} \mu_{ij}^{\hat{m}} \tag{17}$$

in which, $\hat{C}^{\hat{m}}$ denotes the instantaneous plastic modulus associated with the current active yield surface expressed as:

$$\hat{C}^{\hat{m}} = C^{\hat{m}} \mu_{ij}^{\hat{m}} \dot{\varepsilon}_{ij}^{vp} \tag{18}$$

where, $C^{\hat{m}}$ is the plastic modulus of the current active yield surface. The instantaneous plastic modulus is scaled by the magnitude of the projection of the slip rate on to the

translation direction of the active yield surface. This is analogous to the instantaneous modulus in case of single yield surface viscoplasticity, where the plastic modulus is scaled with the magnitude of slip rate. For the yield surfaces that lie outside the current stress state (i.e., $m > \hat{m}$), the backstress remains instantaneously stationary.

In contrast to the rate independent plasticity, where the inner surfaces remain tangent to the active yield surface, the viscoplastic model does not require the stress state to remain within or on the yield surfaces. To ensure consistency, time dependent translation of the active yield surface and the inner yield surfaces must satisfy the collinearity condition at all times. The evolution of backstress for the inner yield surface is expressed as:

$$\dot{\alpha}_{ij}^{m} = \hat{C}^{\hat{m}} \mu_{ij}^{\hat{m}}; \;\; m < \hat{m} \tag{19}$$

which implies that all inner yield surfaces translate at the same speed and direction with the current active yield surface. This restriction guarantees that there is no relative translation among the inner surfaces until the active yield surface $\hat{m}$ reaches the stress point. Figure 3 illustrates the hardening evolution processes during a creep test. The figure demonstrates the evolution of the yield surfaces under a prescribed deviatoric stress, $\boldsymbol{s}$ at four time instances $t_1 < t_2 < t_3 < t_4$. For simplicity, only the active yield surface and the surface immediately in and out of the active yield surface are depicted in the figure. At time t_1, the stress state remains outside the current active yield surface (i.e., $f^m > 0 \;\forall\; m \leqslant \hat{m}$), which leads to viscoplastic flow. The translation of yield surfaces $m \leqslant \hat{m}$ proceeds along the direction and speed dictated by the current active yield surface, $\hat{m}$, at time t_2. When $f^{\hat{m}}$ vanishes, the inner surface becomes the active yield surface (i.e., $\hat{m} \leftarrow \hat{m} - 1$) and the flow is dictated by the new, active yield surface at time t_3. The flow process proceeds until all inner yield surfaces become tangent at the current stress point.

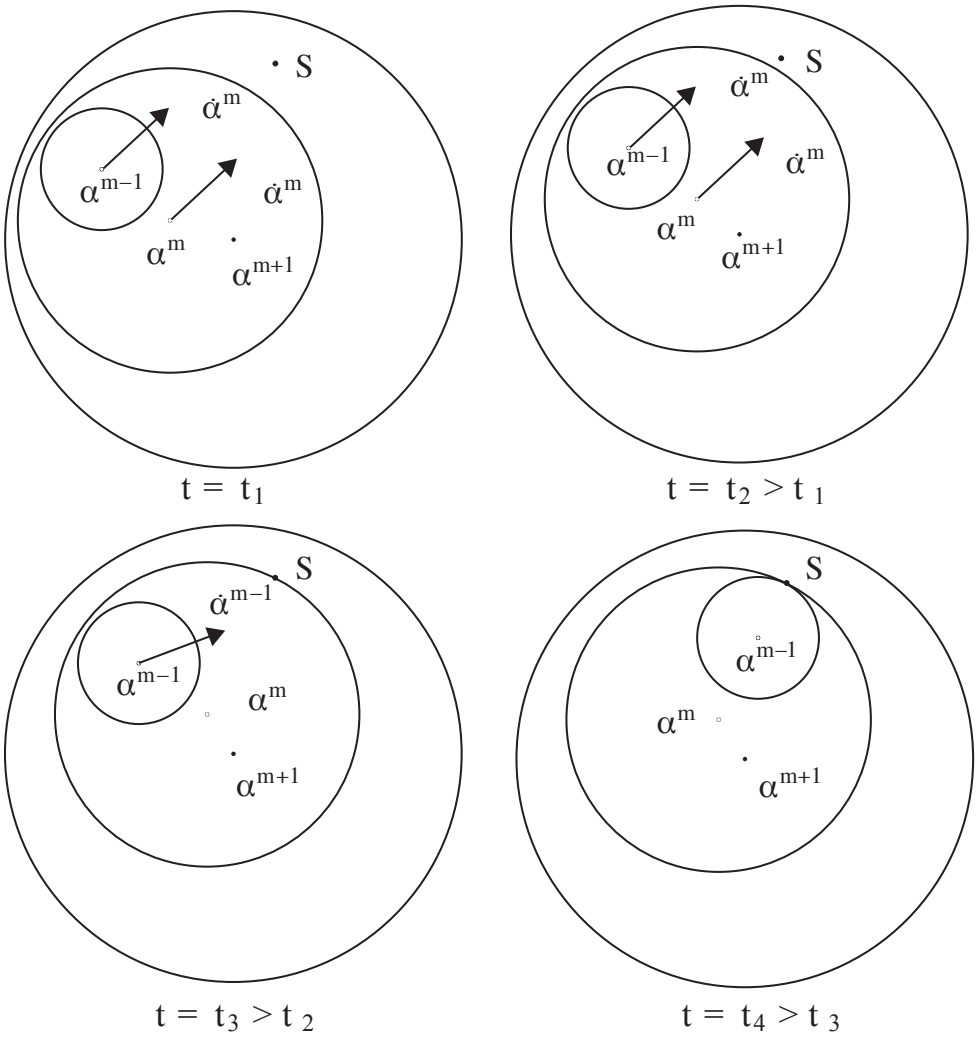

Figure 3: Inner yield surface translation process depicted at four time instances during a creep process.

4 Viscoelastic-viscoplastic model for cyclic deformation at high temperature

In this section, a viscoelastic-viscoplastic model is formulated to capture the cyclic behavior of metals in high temperature environment. The viscoelastic behavior is modeled based on the Boltzmann integral and Prony series approximation of the time dependent moduli. The viscoplastic behavior is modeled using the multi-yield surface viscoplastic model described in Section 3. The purpose of the proposed model is to accurately idealize the cyclic response in high temperature environment, where rate dependence of the response is non trivial. The proposed model builds on the viscoelastic-viscoplastic model previously developed by the authors [31, 37], and extends the formulation to describe the cyclic behavior using the multi-yield surface viscoplasticity framework.

The governing equilibrium equations describing the mechanical response of a body occupying domain $\Omega \subset \mathbb{R}^{n_{\text{sd}}}$ are expressed in the following form:

$$s_{ij,j}\left(\mathbf{x},t\right) - p_{,i}\left(\mathbf{x},t\right) + b_i\left(\mathbf{x},t\right) = 0; \;\; \mathbf{x} \subset \Omega; \;\; t \in [0,t_0] \tag{20}$$

where, $\mathbf{b}$ is the body force per unit volume, $\mathbf{x}$ and t parameterize the spatial and temporal dimensions, respectively, and t_0 is the upper limit of the time domain. The following boundary conditions are prescribed:

$$u_i\left(\mathbf{x},t\right) = \bar{u}_i\left(\mathbf{x},t\right) \quad \mathbf{x} \in \Gamma_D, \;\; t \in [0,t_0] \tag{21}$$

$$\sigma_{ij} n_j = \bar{t}_i\left(\mathbf{x},t\right) \quad \mathbf{x} \in \Gamma_N, \;\; t \in [0,t_0] \tag{22}$$

where, $\mathbf{u}$ denotes the displacement field; $\bar{\mathbf{u}}$ is the prescribed displacement along the Dirichlet boundary; $\Gamma_D \subset \Gamma \equiv \partial\Omega$; $\bar{\mathbf{t}}$ the prescribed traction along the Neumann boundary, $\Gamma_N \subset \Gamma$, such that $\Gamma_D \cap \Gamma_N = \emptyset$ and $\Gamma_D \cup \Gamma_N = \Gamma$; and $\mathbf{n}$ the outer unit normal to the traction boundary.

Assuming small strain kinematics, the total strain tensor, $\boldsymbol{\varepsilon}$, is:

$$\varepsilon_{ij}\left(\mathbf{x},t\right)=\frac{1}{2}\left(u_{i,j}\left(\mathbf{x},t\right)+u_{j,i}\left(\mathbf{x},t\right)\right) \tag{23}$$

The adoption of the small strain theory implies that large rotations and large plastic deformations that may be present in some high temperature applications are not addressed in this study. The total strain tensor is additively split into three components:

$$\varepsilon_{ij}=\varepsilon_{ij}^{\mathrm{ve}}+\varepsilon_{ij}^{\mathrm{vp}}+\varepsilon_{ij}^{\mathrm{T}} \tag{24}$$

$\boldsymbol{\varepsilon}^{\mathrm{ve}}$, $\boldsymbol{\varepsilon}^{\mathrm{vp}}$ and $\boldsymbol{\varepsilon}^{\mathrm{T}}$ respectively denote the viscoelastic, viscoplastic and thermal induced strain.

4.1 Modeling viscoelasticity

The constitutive relationship between the deviatoric stress and the viscoelastic strain is modeled using the Boltzmann superposition integral in the context of linear viscoelasticity:

$$s_{ij}\left(t\right)=\int_{0}^{t}L_{ijkl}^{'}\left(t-\tau\right)\frac{d\varepsilon_{kl}^{\mathrm{ve}}\left(\tau\right)}{d\tau}d\tau \tag{25}$$

in which, the spatial dependence of the pertinent fields is suppressed for simplicity. $\mathbf{L}'$ is the time-dependent deviatoric component of the tensor of viscoelastic moduli, taken to be symmetric and positive definite at any time during the deformation process:

$$L_{ijkl}^{\prime}=L_{klij}^{\prime}=L_{jikl}^{\prime}=L_{ijlk}^{\prime} \tag{26}$$

$$\zeta_{ij}L_{ijkl}^{\prime}\zeta_{kl}\geq\eta\zeta_{ij}\zeta_{ij};\quad\forall\zeta_{ij}=\zeta_{ji};\quad\eta>0 \tag{27}$$

A convenient time evolution expression for the viscoelastic moduli is the Prony series:

$$L_{ijkl}^{\prime}\left(t\right)=\left[K_{e}+\sum_{me=1}^{ME}K_{me}\exp\left(-\frac{t}{\xi_{me}}\right)\right]\bar{L}_{ijkl}^{\prime} \tag{28}$$

in which, $\bar{\mathbf{L}}'$ is the initial moduli tensor; ME the number of Maxwell elements incorporated in the viscoelastic model; K_e denotes the ratio of equilibrium deviatoric moduli over

instantaneous deviatoric moduli; and K_{me} and ξ_{me} are the ratio of deviatoric moduli on me^{th} Maxwell element over instantaneous deviatoric moduli and the time parameters associated with the me^{th} Maxwell element, respectively. Prony series approximation is utilized to generate a component-dependent relaxation. In order to make time independent moduli tensor the instantaneous elastic moduli; i.e., $\bar{\mathbf{L}}' = \mathbf{L}'(t=0)$, the values of the Prony series parameters are constrained such that $K_e + \sum_{me=1}^{M} K_{me} = 1$,

For an isotropic solid, the deviatoric component of the elastic moduli is expressed as:

$$L'_{ijkl}(t) = 2G(t)\left(\delta_{ik}\delta_{jl} - \frac{1}{3}\delta_{ij}\delta_{kl}\right) \tag{29}$$

Substituting Eqs. 28 and 29 into Eq. 25, the deviatoric stress tensor becomes:

$$s_{ij}(t) = 2\bar{G}K_e\varepsilon_{ij}^{\text{ve}}(t) + 2\bar{G}\sum_{me=1}^{ME} K_{me}\varepsilon_{ij}^{me}(t) \tag{30}$$

where,

$$\varepsilon_{ij}^{me}(t) = \int_0^t \exp\left(-\frac{t-\tau}{\xi_{me}}\right)\frac{d\varepsilon_{ij}^{\text{ve}}(\tau)}{d\tau}d\tau \tag{31}$$

in which, $\boldsymbol{\varepsilon}^{\text{ve}}$ is the viscoelastic strain, and $\bar{G} = G(0)$ the instantaneous shear modulus.

The variation of the relaxation behavior as a function of temperature is modeled using the Williams-Landel-Ferry (WLF) equation. Let a_T denote the WLF time-temperature shift factor expressed in the form:

$$\log a_T(T) = \frac{-C_1(T - T_{\text{ref}})}{C_2 + (T - T_{\text{ref}})} \tag{32}$$

where, T denotes temperature; C_1 and C_2 are material constants and T_{ref} is the reference temperature, typically taken to be the room temperature. Provided that the relaxation behavior at the reference temperature and the material constants are known, the relaxation behavior at an arbitrary temperature is obtained by shifting the time scale within a master WLF curve using a_T:

$$t = \int_0^{\tau} \frac{d\xi}{a_T(T(\xi))} \tag{33}$$

where ξ is dummy time variable and τ is the upper limit of temperature variation, the

thermal strains are taken to be volumetric:

$$\varepsilon_{ij}^{\mathrm{T}} = \alpha \left(T - T_{\mathrm{ref}}\right) \delta_{ij} \tag{34}$$

where, α is the thermal expansion coefficient. The viscoplastic strain is taken to remain in the deviatoric strain space (i.e., $\mathrm{tr}(\boldsymbol{\varepsilon}^{\mathrm{vp}}) = 0$). Considering an isotropic solid with insignificant relaxation under hydrostatic loading, the constitutive relationship for pressure becomes:

$$p\left(t\right) = -k u_{i,i}\left(t\right) + 3k\left[\alpha\left(T\left(t\right) - T_0\right)\right] \tag{35}$$

in which, k is the bulk modulus.

4.2 Temperature dependent yielding

The viscoplastic behavior of the material is idealized based on the model defined in Section 3. The viscoplastic hardening exponent, q, is expressed as a function of the non-dimensional temperature, $T^{\star}$, as:

$$q\left(T^{\star}\right) = q_{\mathrm{ref}} + (\bar{q} - q_{\mathrm{ref}}) T^{\star}; \quad T^{\star} = \frac{T - T_{\mathrm{ref}}}{\bar{T} - T_{\mathrm{ref}}} \tag{36}$$

where $q_{\mathrm{ref}} = q(T_{\mathrm{ref}})$ and $\bar{q} = q(\bar{T})$ are exponents evaluated based on experiments performed at two temperatures.

In the multi-yield surface model, the yield stress and the plastic moduli values of each yield surface need to be identified using experimental data. At a given temperature $T^{\star}$, where experimental data is available, the yield strength associated with each yield surface is chosen by linearly spacing the yield functions using the experimentally observed stress - strain relationship:

$$\sigma_Y^m\left(T^{\star}\right) = \sigma_Y^1\left(T^{\star}\right) + \frac{(m-1)\left(\sigma_Y^M\left(T^{\star}\right) - \sigma_Y^1\left(T^{\star}\right)\right)}{M-1} \tag{37}$$

where, M is the total number of the yield surfaces, $\sigma_Y^1\left(T^{\star}\right)$ is the yield strength of the first yield surface and $\sigma_Y^M\left(T^{\star}\right)$ is the yield strength of the Mth yield surface as observed in the

experiments. We note that Eq. 37 does not include an approximation, but a sampling of flow stress from the experimental stress strain curves. The plastic modulus associated with each surface, along with the yield surface strength, fully defines the flow behavior. The plastic moduli $C_m\left(T^\star\right)$ that controls the hardening rate is obtained by minimizing the discrepancy between experimental and simulated stress -strain behavior.

Particularly in the context of thermomechanical cycling, it is necessary to establish the variation of flow stress evolution as a function of temperature. Leveraging the piecewise linear approximation idea of the multi-yield surface plasticity theory, we approximate the temperature variation of flow stress evolution characteristics as piecewise linear as well. Consider a set of stress-strain data at temperatures $\{T_i^\star; T_i < T_{i+1} | i = 1, ..., N_{\text{test}}\}$, where N_{test} denotes number of experiments. Then for any $T_i^\star \leqslant T^\star \leqslant T_{i+1}^\star$, the yield strength and plastic modulus are:

$$\sigma_Y^m\left(T^\star\right) = \sigma_Y^m\left(T_i^\star\right) + \left(\sigma_Y^m\left(T_j^\star\right) - \sigma_Y^m\left(T_i^\star\right)\right) \frac{T^\star - T_i^\star}{T_j^\star - T_i^\star} \tag{38}$$

and

$$C^m\left(T^\star, \sigma_Y^m\right) = C^m\left(T_i^\star, \sigma_Y^m\right) + \left(C^m\left(T_j^\star, \sigma_Y^m\right) - C^m\left(T_i^\star, \sigma_Y^m\right)\right) \frac{T^\star - T_i^\star}{T_j^\star - T_i^\star} \tag{39}$$

It may be possible to employ more elaborate functional forms to idealize the temperature variation of flow evolution compared to Eq. 38 and Eq. 39. The accuracy of the above approximations is clearly controlled by the number and temperature ranges of the experiments.

5 Numerical Implementation

This section provides the details of the mixed finite element formulation and implementation of the viscoelastic-viscoplastic cyclic plasticity model, as well as the implementation algorithm of the multi-yield surface viscoplasticity model. Isothermal conditions are assumed and the thermal state of the system is regarded as input to the deformation problem. Thermal transients were taken to be insignificant at time scales and loading conditions considered in this manuscript.

5.1 Mixed FEM formulation

The system of equations for idealizing the viscoelastic-viscoplastic behavior is numerically evaluated based on the mixed finite element method. In this approach, both displacement and pressure fields are taken to be the cardinal unknowns (as opposed to the standard finite element method, where the displacement field is the sole unknown field and stress is computed at quadrature points). In the current mixed formulation, the nodal displacement and pressure are simultaneously evaluated as described below.

The weak forms of the governing equations of equilibrium in terms of the deviatoric stress and pressure (i.e., Eqs. 20 and 35, respectively) are expressed as:

$$\int_{\Omega} \nu^h_{i,j} s_{ij} d\Omega - \int_{\Omega} \nu^h_{i,i} p d\Omega - \int_{\Gamma^u_N} \nu^h_i \bar{t}_i d\Gamma - \int_{\Omega} \nu^h_i b_i d\Omega = 0 \tag{40}$$

$$\int_{\Omega} \frac{1}{k} q^h p^h d\Omega + \int_{\Omega} q^h u^h_{i,i} d\Omega d\Omega = 0 \tag{41}$$

where, $\mathbf{v}$ and q are the test functions for displacement and pressure, defined within the appropriate Sobolev spaces and with sufficient smoothness, and Let $\mathbf{v}^h$ and q^h belong to the corresponding finite dimensional subspaces of the test functions, $\mathbf{v}$ and q, respectively. We perform a Bubnov-Galerkin discretization of the displacement and pressure fields, as well as the corresponding test functions:

$$u^h_i(\mathbf{x}, t) = \sum_{a=1}^{n_u} N^u_a(\mathbf{x}) \hat{u}_{ai}(t) \tag{42}$$

$$p^h(\mathbf{x}, t) = \sum_{a=1}^{n_p} N^p_a(\mathbf{x}) \hat{p}_a(t) \tag{43}$$

in which, N^u_a and N^p_a are respectively the basis functions of the displacement and pressure fields that correspond to node a; $\hat{(\cdot)}$ denotes the nodal coefficients of the corresponding field; and n_u and n_p are the total number of displacement and pressure nodes, respectively.

Substituting Eqs. 42 and 43 into Eqs. 40 and 41, respectively, the discretized equilibrium

equations take the form:

$$\Psi_{bi} := \int_\Omega N^u_{b,j} s_{ij} d\Omega - \sum_{c=1}^{n_p} \int_\Omega N^u_{b,i} N^p_c d\Omega \hat{p}_c - \int_{\Gamma_N} N^u_b \bar{t}_i d\Gamma \\ - \int_\Omega N^u_b b_i d\Omega = 0; \quad b = 1, ..., n_u \quad (44)$$

$$\Theta_c := \sum_{a=1}^{n_p} \int_\Omega \frac{1}{k} N^p_c N^p_a d\Omega \hat{p}_a + \sum_{b=1}^{n_u} \int_\Omega N^p_c N^u_{b,i} d\Omega \hat{u}_{bi} \\ - \int_\Omega 3 N^p_c [\alpha (T - T_0)] d\Omega = 0; \quad c = 1, ..., n_p \quad (45)$$

Differentiating Eq. 30 in time, employing Eq. 31 and discretizing in time yields the recurrence formula of the deviatoric stress tensor as:

$${}_{t+\Delta t}s_{ij} - {}_t s_{ij} = 2\bar{G} \left({}_{t+\Delta t}\varepsilon^{\text{ve}}_{ij} - {}_t \varepsilon^{\text{ve}}_{ij} \right) \bar{K} - 2\bar{G} \sum_{me}^{ME} K_{me} \left(1 - \exp\left(-\frac{\Delta t}{\xi_{me}} \right) \right) {}_t\varepsilon^{me}_{ij} \quad (46)$$

where,

$$\bar{K} = K_e + \sum_{me}^{ME} K_{me} \left(1 - \exp\left(-\frac{\Delta t}{\xi_{me}} \right) \right) \frac{\xi_{me}}{\Delta t} \quad (47)$$

The left subscript indicates the value of the fields evaluated at discrete time points. Equation 46 indicates that the calculation of the deviatoric stress at current time step requires the strain value at the previous time step only, rather than its entire history as Eq. 31 implies.

Consider a one-parameter discretization of the viscoplastic strain rate in the form:

$$\frac{{}_{t+\Delta t}\varepsilon^{\text{vp}}_{ij} - {}_t \varepsilon^{\text{vp}}_{ij}}{\Delta t} = \theta \, {}_{t+\Delta t}\dot{\varepsilon}^{\text{vp}}_{ij} + (1 - \theta) \, {}_t\dot{\varepsilon}^{\text{vp}}_{ij} \quad (48)$$

in which, $\theta \in [0, 1]$ is an algorithmic parameter. The choices of $\theta = 0, 1$ and 0.5 correspond to the explicit, implicit and midpoint rules, respectively. Substituting Eqs. 24 and 42 into Eq. 46 and using Eq. 48, the discretized form of the constitutive equation for the deviatoric

stress is expressed as:

$$R_{ij} :=_{t+\Delta t} s_{ij} -_t s_{ij} - 2\bar{G}\sum_{a=1}^{n_u} N^u_{a,j}(\mathbf{x})\,{}_{t+\Delta t}\hat{u}_{ai}\bar{K} + 2\bar{G}\sum_{a=1}^{n_u} N^u_{a,j}(\mathbf{x})\,{}_t\hat{u}_{ai}\bar{K}$$
$$+ 2\bar{G}\Delta t\theta_{t+\Delta t}\dot{\varepsilon}^{\mathrm{vp}}_{ij}\bar{K} + 2\bar{G}\Delta t(1-\theta)_t\,\dot{\varepsilon}^{\mathrm{vp}}_{ij}\bar{K} + 2\bar{G}\sum_{me}^{ME} K_{me}\left(1-\exp\left(-\frac{\Delta t}{\xi_{me}}\right)\right){}_t\varepsilon^{me}_{ij} \quad (49)$$

Using Eqs. 17, 19 and 48, the discretized form of the constitutive equation for the backstress of the mth yield surface is expressed as:

$$R^m_{ij} :=_{t+\Delta t} \alpha^m_{ij} -_t \alpha^m_{ij} -_{t+\Delta t} C^{\hat{m}}\Delta t\theta\left({}_{t+\Delta t}\mu^{\hat{m}}_{ij}\right)\left({}_{t+\Delta t}\mu^{\hat{m}}_{kl}\right)\left({}_{t+\Delta t}\dot{\varepsilon}^{\mathrm{vp}}_{kl}\right)$$
$$-_t C^{\hat{m}}\Delta t(1-\theta)\left({}_t\mu^{\hat{m}}_{ij}\right)\left({}_t\mu^{\hat{m}}_{kl}\right)\left({}_t\dot{\varepsilon}^{\mathrm{vp}}_{ij}\right) \quad (50)$$

Equations 44, 45, 49 and 50 together consist of the discretized nonlinear system of the viscoelastic-viscoplastic deformation problem. Newton's method is employed to solve the system of equations [23]. Considering the first order Taylor-series expansion of all four equations:

$${}^{k+1}\Psi_{bi} \approx {}^k\Psi_{bi} + {}^k\left(\frac{\partial\Psi_{bi}}{\partial s_{kl}}\right){}^{k+1}\delta s_{kl} + \sum_{c=1}^{n_p}{}^k\left(\frac{\partial\Psi_{bi}}{\partial\hat{p}_c}\right){}^{k+1}\delta\hat{p}_c$$
$$= {}^k\Psi_{bi} + \int_\Omega N^u_{b,j}\,{}^{k+1}\delta s_{ij}d\Omega - \sum_{c=1}^{n_p}\int_\Omega N^u_{b,i}N^p_c d\Omega\,{}^{k+1}\delta\hat{p}_c = 0 \quad (51)$$

$${}^{k+1}\Theta_c \approx {}^k\Theta_c + \sum_{b=1}^{n_u}{}^k\left(\frac{\partial\Theta_c}{\partial\hat{u}_{bk}}\right){}^{k+1}\delta\hat{u}_{bk} + \sum_{a=1}^{n_p}{}^k\left(\frac{\partial\Theta_c}{\partial\hat{p}_a}\right){}^{k+1}\delta\hat{p}_a$$
$$= {}^k\Theta_c + \sum_{b=1}^{n_u}\int_\Omega N^p_c N^u_{b,i}d\Omega\,{}^{k+1}\delta\hat{u}_{bi} + \sum_{a=1}^{n_p}\int_\Omega\frac{1}{k}N^p_c N^p_a d\Omega\,{}^{k+1}\delta\hat{p}_a = 0 \quad (52)$$

$${}^{k+1}R_{ij} \approx {}^kR_{ij} + {}^k\left(\frac{\partial R_{ij}}{\partial s_{kl}}\right){}^{k+1}\delta s_{kl} + \sum_{a=1}^{n_u}{}^k\left(\frac{\partial R_{ij}}{\partial\hat{u}_{ak}}\right){}^{k+1}\delta\hat{u}_{ak}$$
$$= {}^kR_{ij} - 2\bar{G}\bar{K}\sum_{a=1}^{n_u} N^u_{a,j}\,{}^{k+1}\delta\hat{u}_{ai} + \left(I_{ijkl} + 2\bar{G}\bar{K}\theta\Delta t\,{}^k\bar{C}_{ijkl}\right){}^{k+1}\delta s_{kl} = 0 \quad (53)$$

$$
\begin{aligned}
{}^{k+1}R_{ij}^{m} &\approx {}^{k}R_{ij}^{m} + {}^{k}\left(\frac{\partial R_{ij}^{m}}{\partial \alpha_{kl}^{m}}\right) {}^{k+1}\delta\alpha_{kl}^{m} \\
&= {}^{k}R_{ij}^{m} + \left(I_{ijkl} - {}^{k}C^{m}\theta\Delta t \left({}^{k}\mu_{ij}^{\hat{m}}\right)\left({}^{k}\mu_{st}^{\hat{m}}\right) {}^{k}\bar{C}_{stkl}^{m}\right) {}^{k+1}\delta\alpha_{kl}^{m} = 0
\end{aligned} \tag{54}
$$

in which, the left superscript denotes the Newton iteration count. The Taylor series expansion is performed about the previous iteration, k. $\delta(\cdot)$ denotes the incremental change in the corresponding response field $(\cdot)$ within the Newton iteration. Incorporating Eq. 14, at each yield surface yields:

$$
\begin{aligned}
{}^{k}\bar{C}_{ijkl}^{m} &= {}^{k}\left(\frac{\partial \dot{\varepsilon}_{ij}^{\mathrm{vp}}}{\partial \alpha_{kl}^{m}}\right) \\
&= -\gamma \left\langle \frac{{}^{k}f^{m}}{{}^{k}\sigma_{Y}^{m}} \right\rangle^{q(T^{\star})} \left(\frac{\sqrt{3}}{2\left({}^{k}\bar{s}^{m}\right)} M_{ijkl} + \left(\frac{q\left(T^{\star}\right)}{{}^{k}f^{m}} - \frac{\sqrt{3}}{3\left({}^{k}\bar{s}^{m}\right)} \right) {}^{k}\left(\frac{\partial f^{m}}{\partial \sigma_{ij}}\right) {}^{k}\left(\frac{\partial f^{m}}{\partial \sigma_{kl}}\right) \right)
\end{aligned} \tag{55}
$$

where:

$$
{}^{k}\bar{C}_{ijkl} = {}^{k}\left(\frac{\partial \dot{\varepsilon}_{ij}^{\mathrm{vp}}}{\partial s_{kl}}\right) = -\sum_{m=1}^{M} {}^{k}\bar{C}_{ijkl}^{m} \tag{56}
$$

$$
M_{ijkl} = \delta_{ik}\delta_{jl} - \frac{1}{3}\delta_{ij}\delta_{kl} \tag{57}
$$

The increment of deviatoric stress, ${}^{k+1}\delta s_{ij}$ is evaluated using Eq. 53 as:

$$
{}^{k+1}\delta s_{ij} = {}^{k}Q_{ijkl}\left(2\bar{G}\bar{K}\sum_{a=1}^{n_u} N_{a,l}^{u}\, {}^{k+1}\delta\hat{u}_{ak} - {}^{k}R_{kl}\right) \tag{58}
$$

where, the modulus ${}^{k}\mathbf{Q}$ is defined as:

$$
{}^{k}Q_{ijkl} = \left(I_{ijkl} + 2\bar{G}\bar{K}\theta\Delta t\, {}^{k}\bar{C}_{ijkl}\right)^{-1} \tag{59}
$$

The increment of backstress of the mth yield surface, ${}^{k+1}\delta\alpha_{ij}^{m}$ is evaluated using Eq. 54 as:

$$
{}^{k+1}\delta\alpha_{ij}^{m} = -{}^{k}Q_{ijkl}^{m}\, {}^{k}R_{kl}^{m} \tag{60}
$$

where, the modulus ${}^{k}\mathbf{Q}^{m}$ is defined as:

$$ {}^{k}Q^{m}_{ijkl} = \left(I_{ijkl} - {}^{k}C^{m}\theta\Delta t \, \left({}^{k}\mu^{\hat{m}}_{ij}\right) \left({}^{k}\mu^{\hat{m}}_{st}\right) {}^{k}\bar{C}^{m}_{stkl} \right)^{-1} \tag{61} $$

Substituting Eq. 58 into Eqs. 51 and 52 yield:

$$ \int_{\Omega} 2\bar{G}\bar{K}\, {}^{k}Q_{ijkl} N^{u}_{b,j} \sum_{a=1}^{n_u} N^{u}_{a,l} d\Omega \, {}^{k+1}\delta\hat{u}_{ak} $$

$$ - \sum_{c=1}^{n_p} \int_{\Omega} N^{u}_{b,i} N^{p}_{c} d\Omega \, {}^{k+1}\delta\hat{p}_{c} = \int_{\Omega} {}^{k}Q_{ijkl} N^{u}_{b,j} \, {}^{k}R_{kl} d\Omega - {}^{k}\Psi_{bi} \tag{62} $$

and,

$$ - \sum_{b=1}^{n_u} \int_{\Omega} N^{p}_{c} N^{u}_{b,i} d\Omega \, {}^{k+1}\delta\hat{u}_{bi} - \sum_{a=1}^{n_p} \int_{\Omega} \frac{1}{k} N^{p}_{c} N^{p}_{a} d\Omega \, {}^{k+1}\delta\hat{p}_{a} = {}^{k}\Theta_{c} \tag{63} $$

Equations 62 and 63 are simultaneously evaluated for the increments of the displacement (${}^{k+1}\delta\hat{\mathbf{u}}$) and pressure fields (${}^{k+1}\delta\hat{\mathbf{p}}$) at the current iteration, $k+1$.

When expressed in the matrix form, Eqs. 62 and 63 result in:

$$ \begin{bmatrix} {}^{k}\mathbf{K}^{uu} & \mathbf{K}^{up} \\ (\mathbf{K}^{up})^{T} & \mathbf{K}^{pp} \end{bmatrix} \begin{Bmatrix} {}^{k+1}\delta\hat{\mathbf{u}} \\ {}^{k+1}\delta\hat{\mathbf{p}} \end{Bmatrix} = \begin{Bmatrix} {}^{k}\mathbf{f}^{u} \\ {}^{k}\mathbf{f}^{p} \end{Bmatrix} \tag{64} $$

in which, the components of the tangent stiffness matrix are expressed as:

$$ {}^{k}K^{uu}_{\alpha\beta} = \int_{\Omega} 2\bar{G}\bar{K}\, {}^{k}Q_{ijmn} N^{u}_{b,j} \sum_{a=1}^{n_u} N^{u}_{a,n} d\Omega; \quad \alpha = b + (i-1)\, n_u; \quad \beta = a + (m-1)\, n_u \tag{65} $$

$$ K^{up}_{\alpha c} = - \int_{\Omega} N^{u}_{b,i} N^{p}_{c} d\Omega; \quad \alpha = a + (i-1)\, n_u; \quad 1 \le c \le n_p \tag{66} $$

$$ K^{pp}_{ab} = - \int_{\Omega} \frac{1}{k} N^{p}_{a} N^{p}_{b} d\Omega; \quad 1 \le a, b \le n_p \tag{67} $$

The left superscript is included only on the submatrix, $\mathbf{K}^{uu}$, which is the only nonlinear part of the tangent stiffness matrix. The unknown displacement and pressure coefficients, as well

as the force vectors are expressed in the vector form as:

$$ {}^{k+1}\delta\hat{\mathbf{u}} = \{{}^{k+1}\hat{u}_1, ..., {}^{k+1}\hat{u}_{n_{\rm sd}\times n_{\rm u}}\}^T; \quad {}^{k}\mathbf{f}^u = \{{}^{k}f^u_1, ..., {}^{k}f^u_{n_{\rm sd}\times n_{\rm u}}\}^T \tag{68} $$

$$ {}^{k+1}\delta\hat{\mathbf{p}} = \{{}^{k+1}\hat{p}_1, ..., {}^{k}\hat{p}_{n_p}\}^T; \quad {}^{k}\mathbf{f}^p = \{{}^{k}f^p_1, ..., {}^{k}f^p_{n_p}\}^T \tag{69} $$

and the components of the force vector are given as:

$$ {}^{k}f^u_\alpha = \int_\Omega {}^{k}Q_{ijkl} N^u_{b,j} \, {}^{k}R_{kl} d\Omega - {}^{k}\Psi_{bi}; \quad \alpha = b + (i-1)\, n_u \tag{70} $$

$$ {}^{k}f^p_a = {}^{k}\Theta_a; \quad 1 \le a \le n_p \tag{71} $$

The finite elements discretizing the displacements and the pressure fields are chosen such that the Babuska-Brezzi stability constraint is satisfied [1, 4]. Ensuring this constraint affects the choice of the pressure and displacement discretization and avoids the potential numerical instability and oscillations observed in the response. In the numerical studies provided in this manuscript, we employ nine-node biquadratic elements to discretize the displacement field, and four-node bilinear elements to discretize the pressure field.

5.2 Implementation algorithm of the multi-yield surface deformation model

Based on the expressions above, the following algorithm is employed to compute the pressure and displacement fields:

Given: At arbitrary time $t + \Delta t$, the state at the previous time step; ${}_t\hat{\mathbf{u}}$, ${}_t\hat{\mathbf{p}}$, ${}_t\mathbf{s}$, ${}_t\alpha$, ${}_t\dot{\boldsymbol{\varepsilon}}^{\rm vp}$ and ${}_t\dot{\boldsymbol{\varepsilon}}^{\rm vp}_m$;

Find: The response at the current step; ${}_{t+\Delta t}\hat{\mathbf{u}}$, ${}_{t+\Delta t}\hat{\mathbf{p}}$.

1. Initiate the algorithm: $k = 0$.

2. Set the initial guesses for the pressure and deformation coefficients at the current increment:

$$ {}^0\hat{\mathbf{u}} = {}_t\hat{\mathbf{u}}; \quad {}^0\hat{\mathbf{p}} = {}_t\hat{\mathbf{p}}; \quad {}^0\mathbf{s} = {}_t\mathbf{s}; \quad {}^0\alpha_m = {}_t\alpha_m; \quad {}^0\dot{\boldsymbol{\varepsilon}}^{\rm vp} = {}_t\dot{\boldsymbol{\varepsilon}}^{\rm vp}; \quad {}^0\dot{\boldsymbol{\varepsilon}}^{\rm vp}_m = {}_t\dot{\boldsymbol{\varepsilon}}^{\rm vp}_m \tag{72} $$

3. Loop until convergence:

   (a) Compute the moduli: $\bar{K}$, ${}^{k}\bar{\mathbf{C}}$, ${}^{k}\mathbf{Q}$, ${}^{k}\bar{\mathbf{C}}^{m}$ and ${}^{k}\mathbf{Q}^{m}$ using Eqs. 47, 56, 59, 55 and 61, respectively at each quadrature point.

   (b) Calculate ${}^{k}\boldsymbol{\Psi}$, ${}^{k}\boldsymbol{\Theta}$ using Eqs. 44, 45, and ${}^{k}\mathbf{R}$, ${}^{k}\mathbf{R}^{m}$ using Eqs.49 and 50, respectively at each quadrature point.

   (c) Update the pressure and displacement increments, ${}^{k+1}\delta\hat{\mathbf{u}}$ and ${}^{k+1}\delta\hat{\mathbf{p}}$ by solving the linear system in Eq. 64.

   (d) Compute deviatoric stress increment ${}^{k+1}\delta\mathbf{s}$ and backstress increment ${}^{k+1}\delta\boldsymbol{\alpha}_m$ at each quadrature point using Eq. 58 and Eq. 60.

   (e) Update displacement, pressure, deviatoric stress and backstress:

$$ {}^{k+1}\hat{\mathbf{u}} = {}^{k+1}\delta\hat{\mathbf{u}} + {}^{k}\hat{\mathbf{u}} \tag{73} $$

$$ {}^{k+1}\hat{\mathbf{p}} = {}^{k+1}\delta\hat{\mathbf{p}} + {}^{k}\hat{\mathbf{p}} \tag{74} $$

$$ {}^{k+1}\mathbf{s} = {}^{k+1}\delta\mathbf{s} + {}^{k}\mathbf{s} \tag{75} $$

$$ {}^{k+1}\alpha^{m} = {}^{k+1}\delta\alpha^{m} + {}^{k}\alpha^{m} \tag{76} $$

   (f) Update viscoplastic strain rate ${}^{k+1}\dot{\boldsymbol{\varepsilon}}^{\mathrm{vp}}$ using Eq. 14.

   (g) Update viscoplastic strain ${}^{k+1}\boldsymbol{\varepsilon}^{\mathrm{vp}}$ by evaluating:

$$ {}^{k+1}\boldsymbol{\varepsilon}^{\mathrm{vp}} = {}_{t}\boldsymbol{\varepsilon}^{\mathrm{vp}} + \theta\Delta t\, {}^{k+1}\dot{\boldsymbol{\varepsilon}}^{\mathrm{vp}} + (1-\theta)\,\Delta t\, {}_{t}\dot{\boldsymbol{\varepsilon}}^{\mathrm{vp}} \tag{77} $$

   (h) Update yield surface translation direction ${}^{k+1}\boldsymbol{\mu}^{m}$ using Eq. 10.

   (i) Check Newton-Raphson method convergence criterion $\frac{\left\|{}^{k+1}\delta\hat{\mathbf{u}}\right\|}{\left\|{}^{k+1}\hat{\mathbf{u}}\right\|}$.

   (j) $k = k + 1$

6 Numerical Investigations

The proposed computational model is employed to investigate the mechanical response of a titanium alloy at elevated temperatures. The alloy of the interest Ti-6Al-2Sn-4Zr-2Mo-

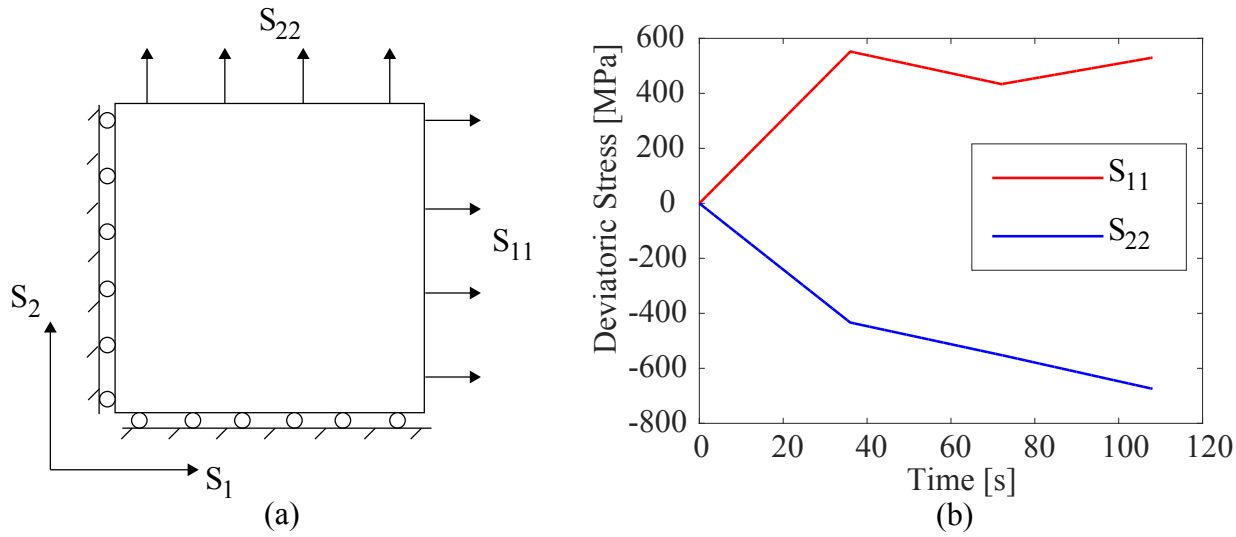

Figure 4: The geometry and loading profile used in the numerical verification study.

0.1Si (Ti-6242S) displays good mechanical properties at elevated temperature, making it a candidate structural material for hypersonic aircraft applications. The present investigations start with the verification of the multi-yield surface viscoplastic model (Section 6.1), where a parametric study is conducted to investigate the effectiveness of the proposed formulation in ensuring that the collinearity rule is strictly enforced. Section 6.2 presents the performance of the proposed model in idealizing the response of Ti-6242S under cyclic, static, and relaxation tests.

6.1 Verification of multi-yield surface viscoplasticity implementation

We consider the response of a specimen loaded in biaxial direction, as illustrated in Fig.4. The lateral stress loading S_{11} is monotonically increased to 550 MPa in 36 s then gradually reduced to 440 MPa until 72 s, after that it increased again to 530 MPa until 108 s. The vertical stress load, S_{22} linearly increases to 435 MPa in the compressive direction in 36 s, then it keeps increasing to 550 MPa monotonically at 108 s. Two simulations are performed and compared to assess the capability of the proposed model in capturing the viscoplastic behavior without violating the collinearity assumption. The first simulation is executed

without the incorporated direction correction term; therefore the backstress evolution in each yield surface follows Prager's linear kinematic hardening rule. The second simulation follows the proposed evolution law as shown in Eq. 17. The evolution of the yield surfaces as a function of time using both models are summarized in Fig. 5. Seven yield surfaces are employed and 3 snapshots are plotted from the yield stress translation process; at 36 s, at 72 s, and at 108 s. The yield surfaces are concentric circles at the beginning of the test. At 36 s, both simulations yield similar outcomes as shown in Fig. 5 (a) and (d), implying the collinearity of the backstress of each yield surface using both approaches. This result is expected since no significant creep is observed during the monotonic loading process in the first 36 seconds of loading. As the stress tensor translates after 36 s due to the change of loading directions, Fig. 5 (b) and (c) clearly begins to demonstrate several intersecting yield surfaces. In contrast, the proposed approach eliminates the intersections as shown in Fig. 5 (e) and (f).

6.2 Simulation of the response of Ti-6242S alloy

The material properties for the viscoelastic and viscoplastic components, as well as the multi-yield surface parameters (e.g., number of yield surfaces, yield stresses, plastic moduli, etc.) of the titanium alloy, Ti-6242S were identified. Model calibration is performed based on the experimental data conducted at the Air Force Research Laboratory, as well as data available in the literature. Due to the temperature dependence of the cyclic test, experiments at varying temperatures are required to generate a complete calibrated model. Due to the limited amount of available data across a wide range of temperature spectrum, the cyclic model is partially calibrated only. We further note that since the proposed model is phenomenological, the purpose of this section is to demonstrate its capabilities in capturing the behavior of metal alloys, rather than assessing predictive capability.

The monotonic elastic and plastic parameters are calibrated based on a series of uniaxial tensile experiments conducted at room temperature, 538^0C, 593^0C and 650^0C, from which the temperature variation of Young's modulus, Poisson's ratio, number of yield surfaces, yield strengths, plastic moduli and strain hardening variable are calibrated. 11 yield surfaces were used to describe the behavior of the alloy, in which the outermost yield surface is set to be

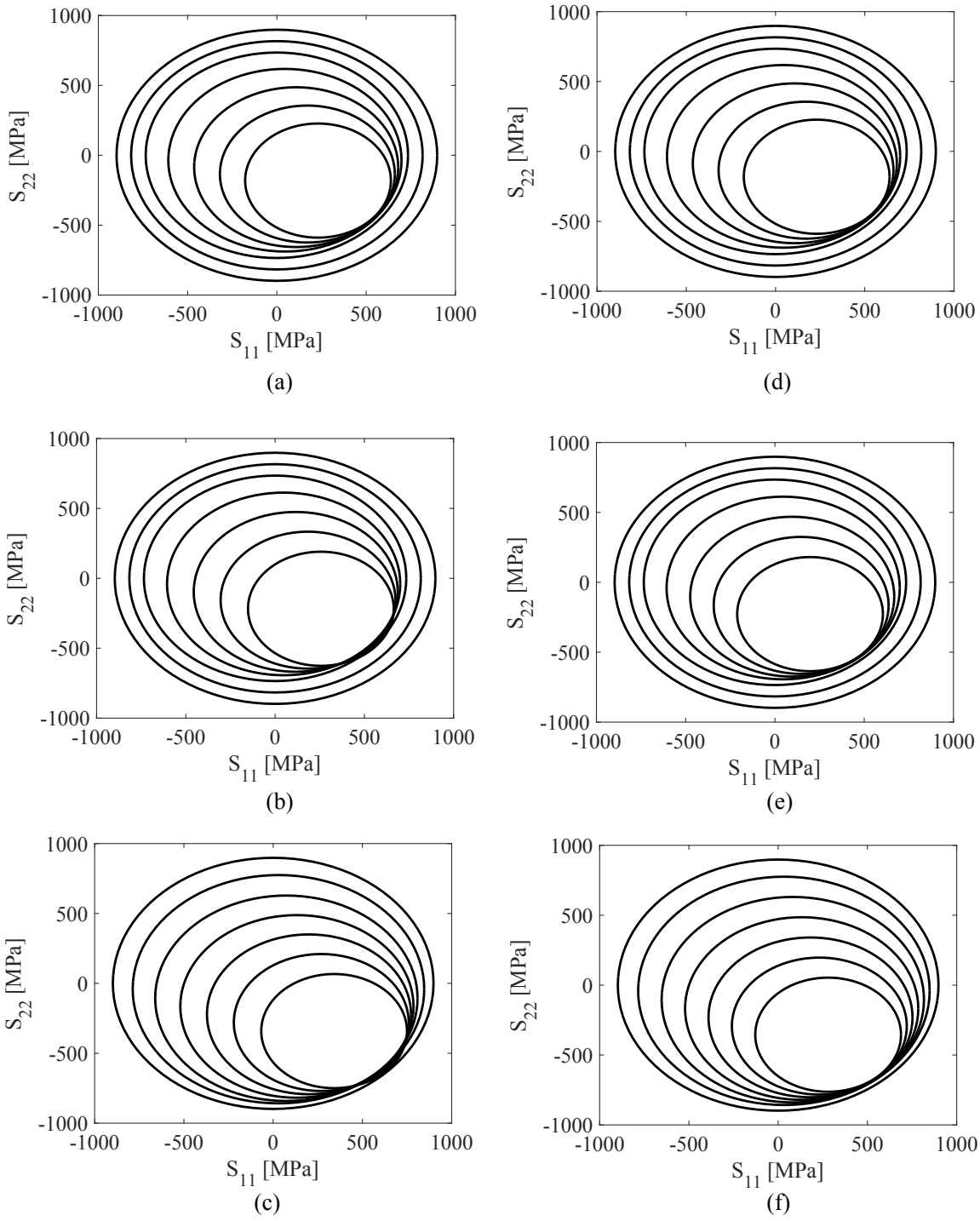

Figure 5: Yield surface translation process of translation direction at times (a) 36 s; (b) 72 s; (c) 108 s without translation correction; and with corrected translation direction at times (d) 36 s; (e) 72 s ; and (f) 108 s.

large enough to ensure that the stress point always remains inside of it. For the initially undamaged material all the yield surfaces are concentric and share the same origin. The material parameters at other temperatures are linearly interpolated or extrapolated from the calibrated parameters at known temperatures. The loading rate effect is investigated at room temperature only, where the viscosity at room temperature was determined. The stress-strain response at high temperatures using the calibrated properties are compared to the experimental measurements in Fig. 6. The proposed approach is capable of accurately representing the stress-strain behavior under the monotonic loading conditions.

The viscoplastic parameters of the multi-yield surface model including the fluidity parameter, γ, the hardening parameters, q_0 and q^*, and the viscoelastic parameters are calibrated based on stress relaxation tests conducted at temperatures of 593^0C and 650^0C. Figure 7 shows the comparisons between the experimentally observed and simulated short term relaxation behavior at temperatures of 593^0C and 650^0C under the constant strain magnitude of 3.5%. During the first 40 seconds of relaxation, both viscoelastic and viscoplastic relaxation processes are active since the specimens were loaded to stress levels beyond the static yield strength. Figures 8 and 9 compare the simulated and observed long-term relaxation behavior up to 100 hours. The long-term relaxation behavior is governed by the viscoelastic component of the model, as the stress drops below the temperature dependent static yield stress. The calibrated model shows a good match with the experiments at the given temperatures.

The cyclic response of Ti-6242S are compared to the experimental data conducted at the Air Force Research Laboratory. The test specimen is a round bar with a cross section diameter of 0.25 in and a gauge length of 1 in. The uniaxial experiments were displacement controlled with a strain range 0.012 and constant strain rate of $1.0e^{-3}$/s. Three tests were performed at high temperature environment: 450 ^{0}C with a strain ratio of -1, 550 ^{0}C with a strain ratio of -∞ and 550 ^{0}C with a strain ratio of -1 accompanied by stress relaxation at the compression side. The test conditions are summarized in Table 1. The plastic moduli are less nonlinear in the low temperature environment and generally require less number of yield surfaces to generate accurate results than in the high temperature environment.

The simulation results at 450 ^{0}C are compared to the experimental results in Fig. 10. The applied strains in the experiment and the simulation are shown in Fig. 10(a), where

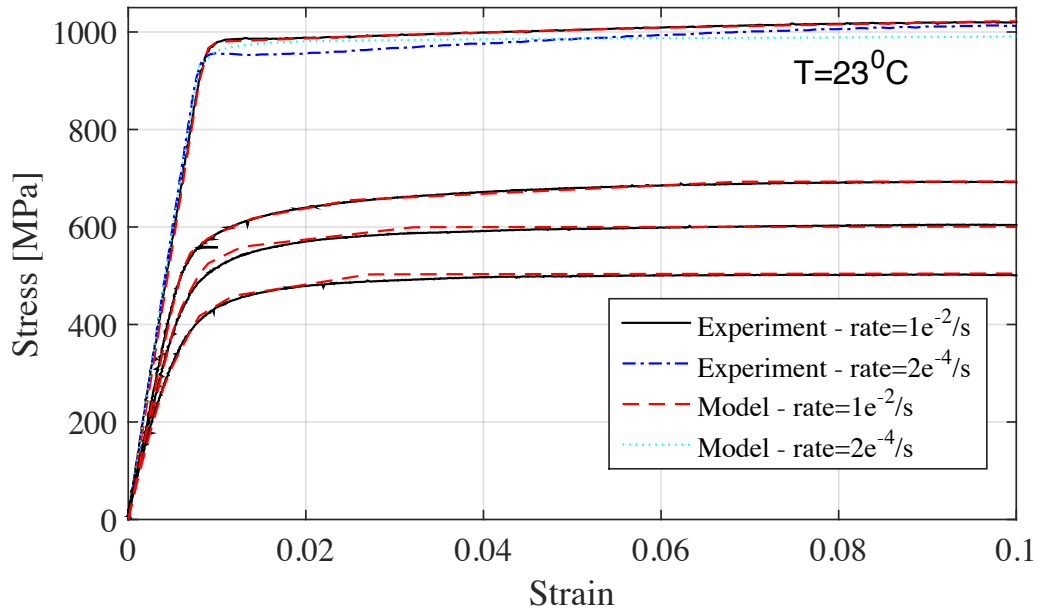

Figure 6: The stress-strain response of Ti-6Al-2Sn-4Zr-2Mo-0.1Si at room and elevated temperatures.

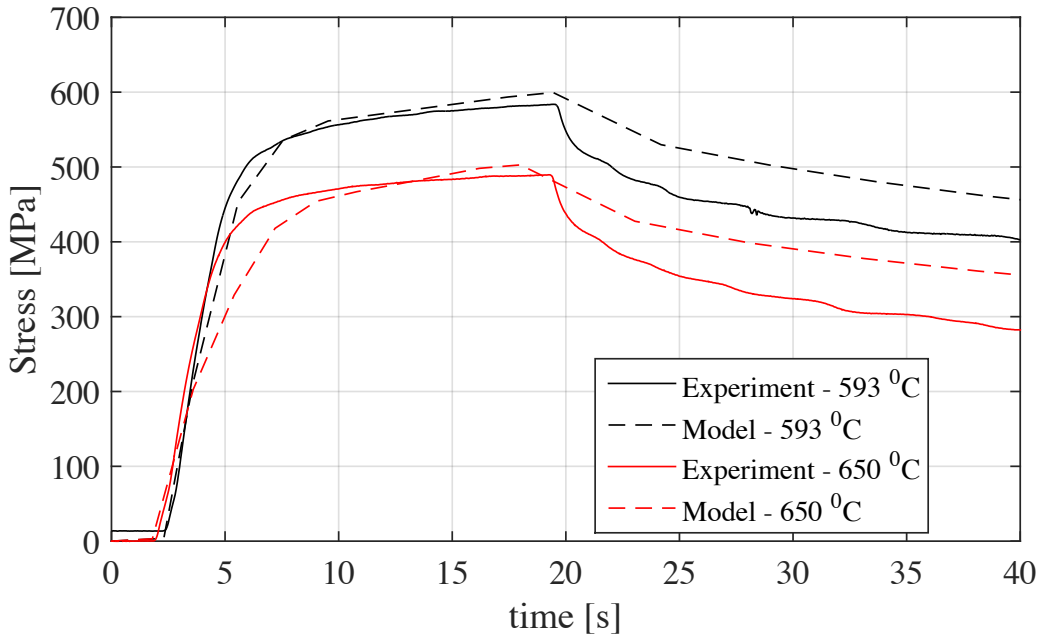

Figure 7: The stress relaxation test of Ti-6Al-2Sn-4Zr-2Mo-0.1Si at 593^{0}C and 650^{0}C for 40 seconds.

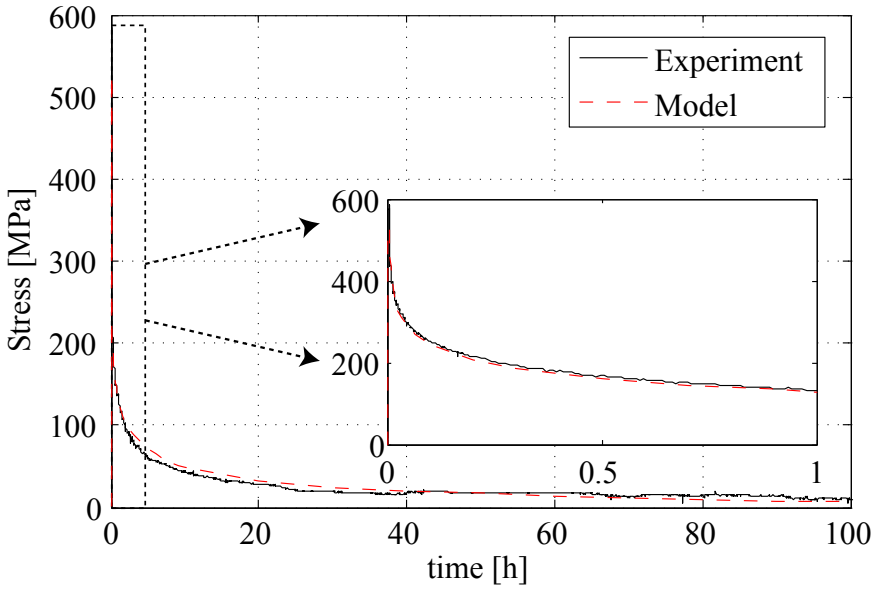

Figure 8: The stress relaxation test of Ti-6Al-2Sn-4Zr-2Mo-0.1Si at 593^0C for 100 hrs.

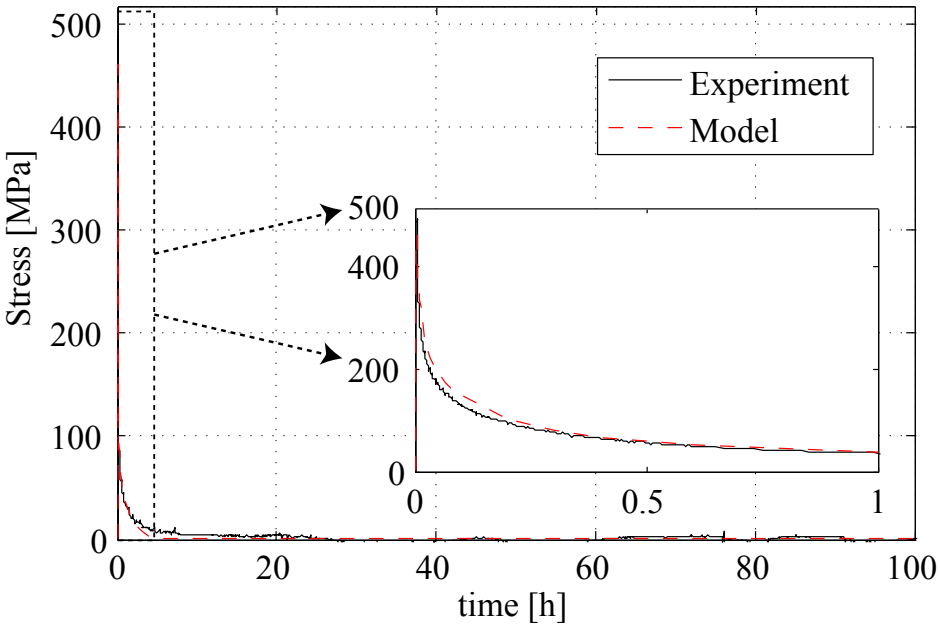

Figure 9: The stress relaxation test of Ti-6Al-2Sn-4Zr-2Mo-0.1Si at 650^0C for 100 hrs.

Table 1: Cyclic test conditions of Ti-6242S.

Experiments	R	$\Delta\varepsilon$	$T\ [^0C]$	$\dot{\varepsilon}$ [1/s]
C1	-1	0.012	450	1.0 e-3
C2	-1	0.012	550	9.6 e-4
C6	$-\infty$	0.012	550	1.0 e-3

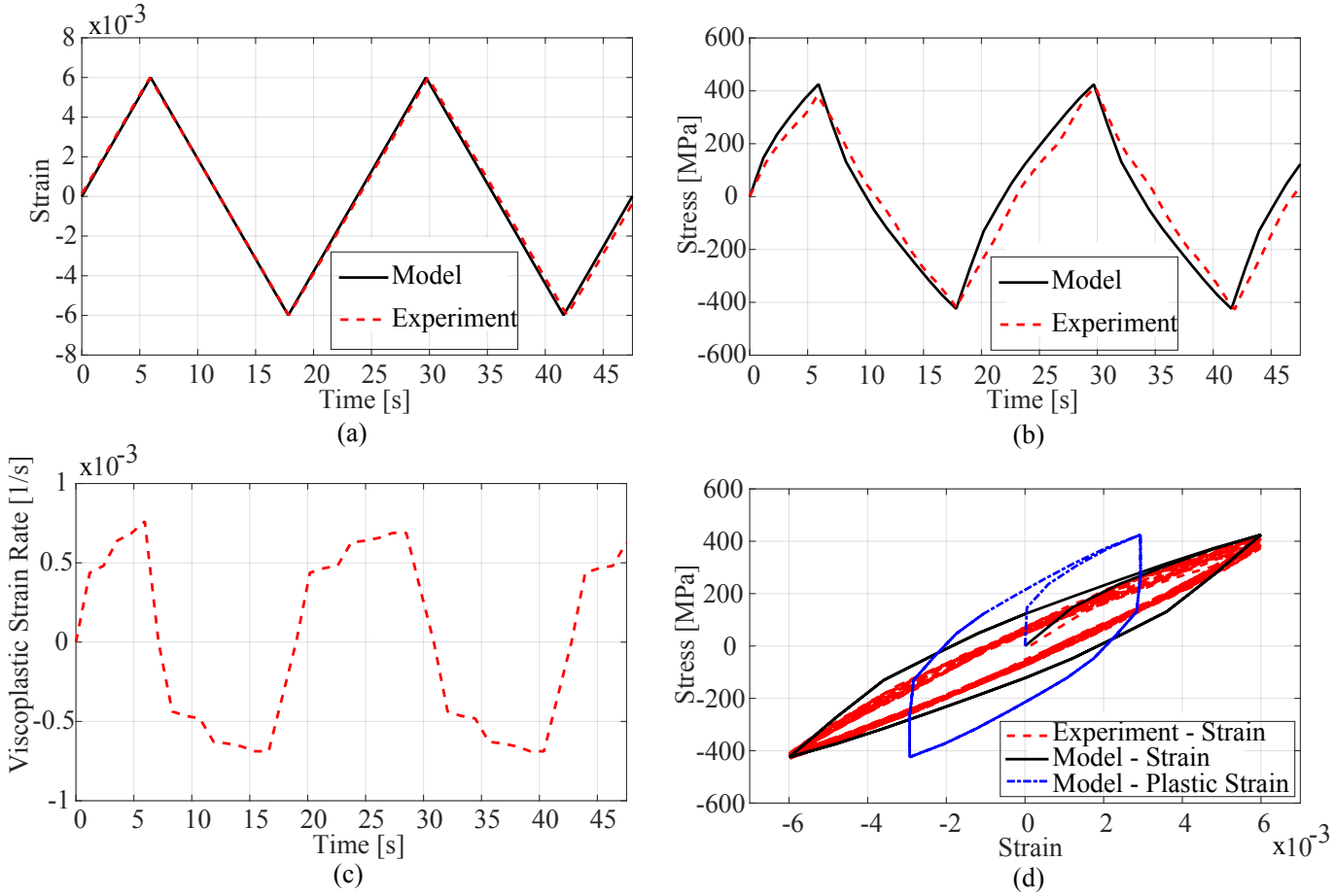

Figure 10: Strain controlled low cycle fatigue test at 450 ^{0}C of (a) simulation and experiment strain input history comparison; (b) simulation and experiment stress history comparison; (c) simulated viscoplastic strain rate history; and (d) simulated stress vs. strain and stress vs. plastic strain comparison.

first two cycles of the test are modeled. The simulated stress presented in Fig. 10(b) is in a good match with the experimental data. The simulated viscoplastic strain rate history is shown in Fig. 10(c), where each section of the viscoplastic strain rate magnitude is a direct consequence of the activation of a new yield surface. The comparison of the experimental and simulated initial hysteresis loop of stress-strain curve and stress-plastic strain curve are shown in Fig. 10(d). The applied 0.6% strain generates approximately 0.3% plastic strain.

Figure 11 shows the results of the simulation and experiments at 550 ^{0}C. The applied strain is shown in Fig. 11(a). The strain range is the same as the test at 450 ^{0}C (1.2%) but with a different R ratio, -∞. The simulated and experimental stress presented in Fig. 11(b)

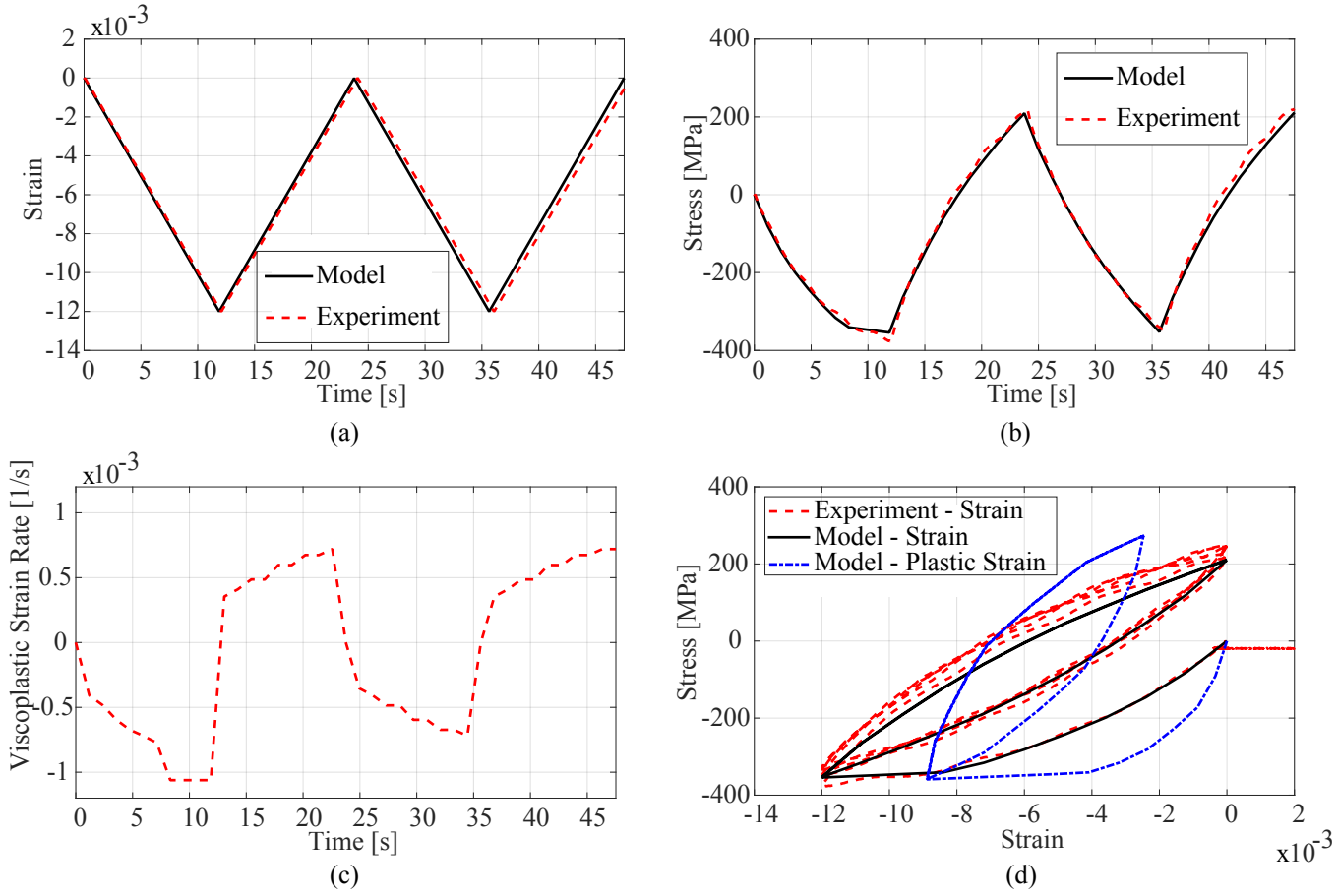

Figure 11: Strain controlled low cycle fatigue test at 550 ^{0}C of (a) simulation and experiment strain input history comparison; (b) simulation and experiment stress history comparison; (c) simulated viscoplastic strain rate history; and (d) stress vs. strain comparison and the simulated stress vs. plastic strain.

shows a more pronouced nonlinearity compared to 450 ^{0}C due to the higher temperature. The simulated viscoplastic strain rate history is presented in Fig. 11(c). The peak value of the viscoplastic strain reduces after the initial loading, as a result of the asymmetric strain ratio. The comparison of the simulated and experimental initial hysteresis loops and stress plastic strain curve are demonstrated in Fig. 11(d). The applied 1.2% strain also generates an approximate 0.6% plastic strain. Eventually the stress, viscoplastic strain rate and stress-strain hysteresis loop are all shifted toward the compression direction due to the applied strain ratio.

Figure 12 demonstrates the results of the creep-fatigue experiment and the corresponding

simulation performed at 550 ^{0}C. The strain hold time of 119 sec was applied following the compression as shown in Fig. 12(a). The simulated and experimental stress time data are presented in Fig. 12(b). The stress relaxation, primarily due to viscoelasticity at high temperature is apparent. While some discrepancy exist between the simulated and experimental relaxation data, the proposed model clearly captures the significant and fast relaxation behavior. The simulated viscoplastic strain rate history is presented in Fig. 12(c), show that the viscoplastic strain rate vanishes shortly after hold as the stress point retreats inside the initial yield surface during the stress relaxation. The comparison of the simulated initial hysteresis loop of stress-strain curve and stress-plastic strain curve are demonstrated in Fig. 12(d). The comparison of the initial experimental and simulation hysteresis loops demonstrates some discrepancy at the initial loading stage, but the simulated behavior is in overall agreement with the experiments.

7 Conclusion

This manuscript provided a multi-yield surface viscoplastic model to study the cyclic response of alloys in high temperature environment, from which the time dependent effect has been addressed on the backstress evolution and the collinearity rule. The computational model was verified in a parametric study and then calibrated against experiments conducted in a variety of temperatures of Ti-6242S. The proposed computational model eliminates the non-smooth intersection of yield surfaces in viscoplastic regime and generates a good match of the hysteresis curve compared to the experiments conducted on Ti-6242S specimens at high temperatures.

The proposed approach is phenomenological in nature and intended to provide a reasonable accurately estimate of the stress and deformation state in structural systems in a computationally efficient manner. The proposed approach, due to its parametric form and flexibility in representing the constitutive behavior, could serve as a macroscale constitutive form for sequential multiscale models, where the parameters and response patterns are obtained directly from lower scale computations (as opposed to relying on experiments for the same purpose [38]).

Prediction of the mechanical and thermo-mechanical fatigue life of viscoplastic materials

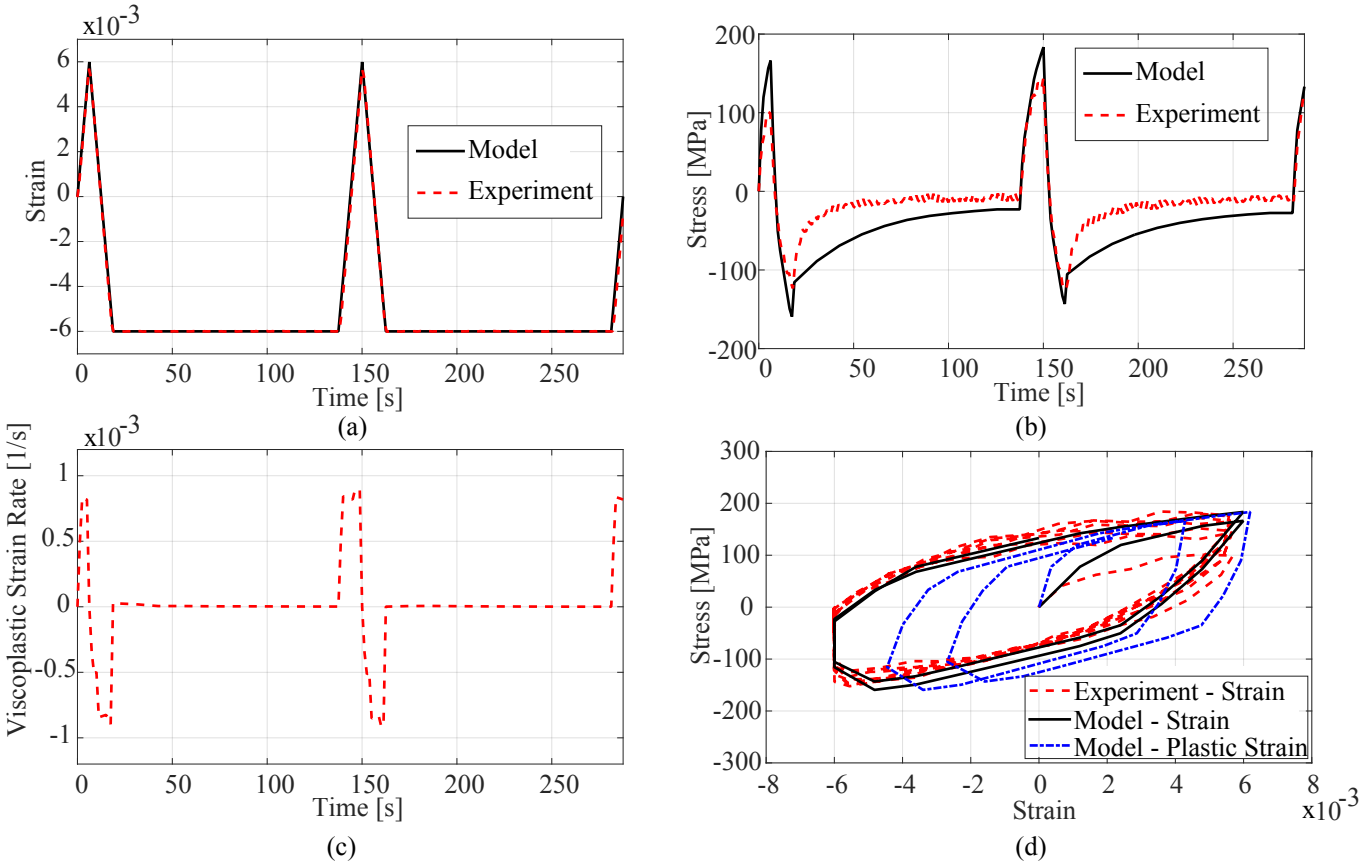

Figure 12: Strain controlled low cycle fatigue stress relaxation test at 550 ^{0}C of (a) simulation and experiment strain input history comparison; (b) simulation and experiment stress history comparison; (c) simulated viscoplastic strain rate history; and (d) stress vs. strain comparison and the simulated stress vs. plastic strain.

at high temperatures are of significant interest and will be investigated in the near future. Several developments on the computational front are needed to achieve such a life prediction capability, particularly for thermo-mechanical loading. First is the extension of the multiple time scale approaches to in-phase and out-of-phase thermo-mechanical load cycles. Presently, the multiple time scale homogenization has been developed in the context of mechanical fatigue alone. Second, modeling long-term degradation requires incorporation of progressive damage models (e.g., continuum damage mechanics or phase field) to the proposed multi-yield surface framework. The near term efforts will focus on the development of these computational capabilities.

8 Acknowledgements

The authors gratefully acknowledge the financial and technical support from the Air Force Research Laboratory, Structural Sciences Center (Contract No: GS04T09DBC0017 through High Performance Technologies, Inc.) and the Air Force Office of Scientific Research Multi-Scale Structural Mechanics and Prognosis Program (Grant No: FA9550-13-1-0104. Program Manager: Dr. David Stargel).

References

[1] I. Babuska. Finite element method with lagrangian multipliers. *Numer. Math.*, 20: 179–192, 1973.

[2] S. Bari and T. Hassan. Anatomy of coupled constitutive models for ratcheting simulation. *Int. J. Plasticity*, 16:381–409, 2000.

[3] M. J. Bogdanor and C. Oskay. Prediction of progressive fatigue damage and failure behavior of IM7/977-3 composites using the reduced-order multiple space-time homogenization approach. *J. Composite Mater.*, 2016.

[4] F. Brezzi. Existence, uniqueness and approximation of saddle- point problems arising from lagrangian multipliers. *Rev. Fr. Automat. Infor.*, 8:129–151, 1974.

[5] E. Busso and F. McClintock. A dislocation mechanics-based crystallographic model of a b2-type intermetallic alloy. *Int. J. Plasticity*, 12:1–28, 1996.

[6] J. L. Chaboche. Constitutive equations for cyclic plasticity and cyclic viscoplasticity. *Int. J. Plasticity*, 5:247–302, 1989.

[7] J. L. Chaboche. A review of some plasticity and viscoplasticity constitutive theories. *Int. J. Plasticity*, 24:1642–1693, 2008.

[8] X. Chen and A. Abel. A two-surface model describing ratchetting behaviors and transient hardening under nonproportional loading. *Acta Mech. Sin.*, 12:368–376, 1966.

[9] D. Y. Chiang and J . L . Beck. A transformation method for implementing classical multi-yield-surface theory using the hardening rule of mroz. *Int. J. Solids Struct.*, 33, 1996.

[10] K. S. Choi and J. Pan. A generalized anisotropic hardening rule based on the mroz multi-yield-surface model for pressure insensitive and sensitive materials. *Int. J. Plasticity*, 25:1325–1358, July 2009.

[11] C. L. Chow and Y. Wei. A model of continuum damage mechanics for fatigue failure. *Int. J. Fatigue*, 50:301–306, 1991.

[12] C. C. Chu. A three-dimensional model of anisotropic hardening in metals and its application to the analysis of sheet metal formability. *J. Mech. Phys. Solids*, 32:197–212, 1984.

[13] R. D. Crouch, C. Oskay, and S. B. Clay. Multiple spatio-temporal scale modeling of composites subjected to cyclic loading. *Comp. Mech.*, 51:93–107, 2013.

[14] R. D. Crouch and C. Oskay. Accelerated time integrator for multiple time scale homogenization. *Int. J. Numer. Meth. Engng.*, 101:1019–1042, 2015.

[15] A. Elgamal, Z. Yang, E. Parra, and A. Ragheb. Modeling of cyclic mobility in saturated cohesion soils. *Int. J. Plasticity*, 19:883–905, 2003.

[16] J. Fish and C. Oskay. A nonlocal multiscale fatigue model. *Mech. Adv. Materials and Structures*, 12:485–500, 2005.

[17] C. O. Frederick and P. J. Armstrong. A mathematical representation of the multiaxial Bauschinger effect. *Mater. High Temp.*, 24:1–26, 2007.

[18] Q. Gu, J. P. Conte, A. Elgamal, and Z. Yang. Finite element response sensitivity analysis of multi-yield-surface J2 plasticity model by direct differentiation method. *Comp. Methods Appl. Mech. Engrg.*, 198:2272–2285, 2009.

[19] Y. Jiang and H. Sehitoglu. Modeling of cyclic ratchetting plasticity, Part I: Development of constitutive relations. *J. Appl. Mech.*, 63:720–725, 1996.

[20] A. Khosravifar. *Analysis and design for inelastic structural response of extended pile shaft foundations in laterally spreading ground during earthquakes*. PhD thesis, University of California Davis, 2012.

[21] B. Klusemann and D. Kochmann. Microstructural pattern formation in finite-deformation single-slip crystal plasticity under cyclic loading: Relaxation vs. gradient plasticity. *Comp. Methods Appl. Mech. Engrg.*, 278:765–793, 2014.

[22] E. Krempl and D. Yao. The viscoplasticity theory based on overstress applied to ratchetting and cyclic hardening. In K.-T. Rie, editor, *Low Cycle Fatigue and Elasto-Plastic Behaviour of Materials*, pages 137–148. Springer Netherlands, 1987.

[23] H. P. Langtangen. *Computational Partial Differential Equations: Numerical Methods and Diffpack Programming*. Springer, 2003.

[24] T. H. Lehmann. Some remarks on a general class of yield conditions for large elasto-plastic deformation. *Ing. Arch.*, 41:297–310, 1972.

[25] L. Li, L. Shen, and G. Proust. Fatigue crack initiation life prediction for aluminum alloy 7075 using crystal plasticity finite element simulations. *Mech. Mater.*, 81:84–93, 2015.

[26] D. L. McDowell. Viscoplasticity of heterogeneous metallic materials. *Mater. Sci. Eng. R*, 62:67–123, 2008.

[27] Z. Mroz. On the description of anisotropic workhardening. *J. Mech. Phys. Solids*, 15: 163–175, 1967.

[28] N. Ohno and J. D. Wang. Kinematic hardening rules with critical state of dynamic recovery .1. Formulation and basic features for ratcheting behavior. *Int. J. Plasticity*, 9:375–390, 1993.

[29] C. Oskay and J. Fish. Fatigue life prediction using 2-scale temporal asymptotic homogenization. *Int. J. Numer. Meth. Engng.*, 61:329–359, 2004.

[30] C. Oskay and J. Fish. Multiscale modeling of fatigue for ductile materials. *Int. J. Comp. Multiscale Engng.*, 2:1–25, 2004.

[31] C. Oskay and M. Haney. Computational modeling of titanium structures subjected to thermo-chemo-mechanical environment. *Int. J. Solids Structures*, 47:3341–3351, 2010.

[32] W. Prager. Recent developments in the mathematical theory of plasticity. *J. Appl. Phys.*, 20:235–241, 1949.

[33] J. Prevost. Plasticity theory for soil stres-strain behavior. *J. Eng. Mech. Div*, 104: 1177–1194, 1978.

[34] J. Prevost. Constitutive equations for soil media. *Proceedings NATO advanced study institute on numerical methods in geomechanics*, pages 79–102, 1981.

[35] J. Prevost. A simple plasticity theory for frictional cohesionless soil. *Soil. Dyn. Earthq. Eng.*, 4:9–17, 1985.

[36] H. Yan and C. Oskay. A three-field (displacement-pressure-concentration) formulation for couled transport-deformation problems. *Finite Elem. Anal. Des.*, 90:20–30, 2014.

[37] H. Yan and C. Oskay. A viscoelastic-viscoplastic model of titanium structures subjected to thermo-chemo-mechanical environment. *Int. J. Solids Structures*, 56-57:29–42, 2015.

[38] S. Zhang and C. Oskay. Variational multiscale enrichment method with mixed boundary conditions for elasto-viscoplastic problems. *Comput. Mech.*, 55:771–787, 2015.

[39] H. Ziegler. A modification of Prager's hardening rule. *Quart. Appl. Math.*, 17:55–65, 1959.